



Comparison of different quasi-static loading conditions of additively manufactured composite hexagonal and auxetic cellular structures

Jin Zhou^{a,b}, Haibao Liu^c, John P. Dear^a, Brian G. Falzon^d, Zafer Kazanci^{e,*}

^a Department of Mechanical Engineering, Imperial College London, London, SW7 2AZ, United Kingdom

^b School of Mechanical Engineering, Xi'an Jiaotong University, Xi'an, Shaanxi 710049, China

^c Centre for Aeronautics, School of Aerospace, Transport and Manufacturing, Cranfield University, Cranfield MK43 0AL, UK

^d School of Engineering, RMIT University, Melbourne, Australia

^e Advanced Composites Research Group, School of Mechanical and Aerospace Engineering, Queen's University Belfast, Belfast, BT9 5AH, United Kingdom

ARTICLE INFO

Keywords:

Auxetic
Cellular structures
Additive manufacturing
3D printing
Energy absorption
Composite

ABSTRACT

Auxetic cellular structures have the potential to revolutionise sandwich panel cores due to their potential superior energy absorption capability. Because of their negative Poisson's ratio, auxetics behave counterintuitively and contract orthogonally under an applied compressive force, resulting in a densification of material in the vicinity of the applied load. This study investigates three cellular structures and compares their compressive energy absorbing characteristics under in-plane and axial loading conditions. Three unit cell topologies are considered; a conventional hexagonal, re-entrant and double arrowhead auxetic structures. The samples were additively manufactured using two different materials, a conventional Nylon and a carbon fibre reinforced composite alternative (Onyx). Finite element simulations are experimentally validated under out of and in-plane loading conditions and the double arrowhead (auxetic) structure is shown to exhibit comparatively superior energy absorption. For the carbon fibre reinforced material, Onyx, the specific energy absorbed by the double arrowhead geometry was 125% and 244% greater than the hexagonal (non-auxetic) and re-entrant (auxetic) structures respectively.

1. Introduction

Honeycombs and other cellular lattices are commonly integrated within lightweight sandwich constructions as they combine good energy absorbing capabilities, specific strength and stiffness. However, conventionally hexagonal honeycomb structures provide stiffness by orientating the cell walls perpendicular to the bonding axis (out-of-plane) [1]. Orientating the cell walls to be parallel to the bonding axis (in-plane) has been shown to provide a lower level of energy absorption however, further research is needed to improve these compressive properties.

The in-plane behaviour of conventional honeycomb cellular structures has been studied extensively for many years under quasi-static and dynamic loading scenarios [2–4]. Recently cellular structures exhibiting auxetic behaviour have been proposed with enhanced in-plane properties compared to conventional honeycombs. The term auxetic is used to describe a subset of meta-materials which exhibit negative Poisson's

ratio [5]. Therefore, under an applied compressive load an auxetic will contract both parallel and perpendicular to the direction of applied loading [6,7]. Auxetic behaviour was first experimentally demonstrated with foams [8], but larger meso- and macroscopic lattices and cellular structures exhibiting auxetic behaviour have since been developed. While an infinite number of unique auxetic unit cells are theoretically possible, some typical topologies are presented in Fig. 1. A variety of these topologies and their variations have been studied for their compressive properties and are reported in literature [9,10].

Studies have identified how a simple alteration of a hexagonal form will enable the creation of a re-entrant auxetic unit. As a result, re-entrant models are among the most commonly researched cellular topologies as they are easily comparable with a conventional hexagonal cell under crushing [9–12]. When compared with an anti-tetra-chiral, the re-entrant structure was found to provide lower energy absorption under quasi-static compression [13,14]. The re-entrant structure has therefore been extensively enhanced to provide greater in-plane stiffness

* Corresponding author at: School of Mechanical and Aerospace Engineering, Queen's University Belfast, Ashby Building, 125 Stranmillis Road, Belfast, BT9 5AH, United Kingdom

E-mail address: z.kazanci@qub.ac.uk (Z. Kazanci).

<https://doi.org/10.1016/j.ijmecsci.2022.108054>

Received 28 November 2022; Accepted 17 December 2022

Available online 24 December 2022

0020-7403/© 2022 The Author(s). Published by Elsevier Ltd. This is an open access article under the CC BY license (<http://creativecommons.org/licenses/by/4.0/>).

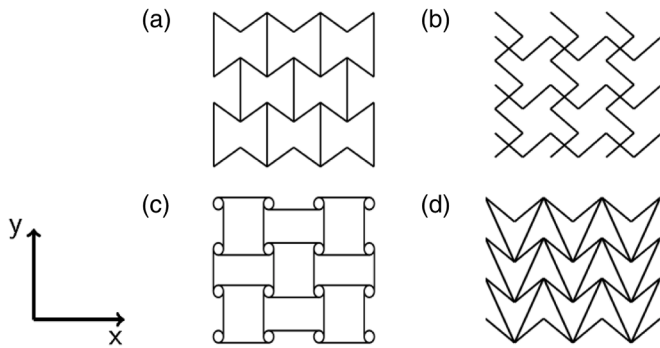


Fig. 1. Auxetic topologies (a) re-entrant, (b) missing rib, (c) anti-tetra-chiral and (d) double arrowhead designs.

and buckling strength [14–17]. While previous studies have primarily focussed on two-dimensional (2D) structures, some studies have investigated the potential improvement offered by three-dimensional (3D) structures [18,19]. Uniform and functionally-graded 2D auxetic double arrowhead honeycombs were assessed for their in-plane energy absorption under compression [20,21]. The 3D form has also been studied and fabricated to investigate the resultant deformation modes under compression [22–24]. These studies do not investigate the comparative performance of a double arrowhead lattice with other auxetic lattices.

Auxetic structures possess geometries which are often difficult to fabricate from conventional structural materials and methods. Metallics have been commonly employed to fabricate auxetic cellular structures [16,23,24]. The advent of 3D printing utilising polymers such as acrylonitrile butadiene styrene and polylactic acid [11,13,15] and the incorporation of reinforcement in these polymers, such as chopped or continuous fibres [25–27], has provided new opportunities for the fabrication of auxetic structures. By combining the enhancements of using auxetic cellular structures and the material enhancements offered through the use of composite materials, there is the opportunity to design and manufacture superior energy absorbing structural cells.

In this study, the quasi-static compressive behaviour of three different cellular topologies (including conventional and auxetic) are investigated under two different loading directions, in-plane and axially.

Samples have been manufactured using 3D printing techniques to compare non-reinforced and reinforced cellular structures under uniaxial compression. Finite element (FE) simulations have been used to compare the deformation and compressive characteristics of each model tested.

2. Sample design and manufacture

Cellular structures may be defined by a number of different parameters and characteristics. These may include the selected unit cell topology, number of cells per unit area, cell wall thicknesses and overall volumetric dimensions. All of these characteristics have the potential to alter the cellular structure mass and properties obtained. For this investigation, the structural capabilities of three different unit cell topologies under quasi-static compression were investigated. These topologies include the non-auxetic hexagonal (HEX), auxetic re-entrant (REE) and double arrowhead (DAH) unit cells. The samples have been designed with 5 unit cells are stacked in the x and y direction within a $50 \times 50 \times 50 \text{ mm}^3$ volume, as shown in

Fig. 2. The associated angle of each unit cell was kept consistent at 120° and a cell wall thickness of 1.1 mm was adopted to satisfy minimum printing requirements. However, printing ordinarily results in shrinkage and so the measured cellular wall thickness varies depending on the printing material selected.

Samples were printed using a Markforged Mark Two 3D printer (Markforged, Watertown, MA, USA) which uses the Fused Filament Fabrication (FFF) printing technique. Two materials have been investigated in this study: unreinforced Nylon and reinforced Nylon (Onyx) which have been denoted as N and O respectively throughout. Onyx is a thermoplastic Nylon which is reinforced with embedded chopped carbon fibre strands (strand length $< 0.1 \text{ mm}$). The resultant composite printing material has a fibre volume fraction of approximately 15% [27]. CAD models were created then sliced using the Markforged cloud slicing software, Eiger (Markforged, Watertown, MA, USA) [28]. Slicing parameters were kept consistent across all samples with a layer height of 0.2 mm and a solid (100%) infill. Therefore, each structure was composed of 250 layers. The printed samples were measured and weighed prior to experimental testing.

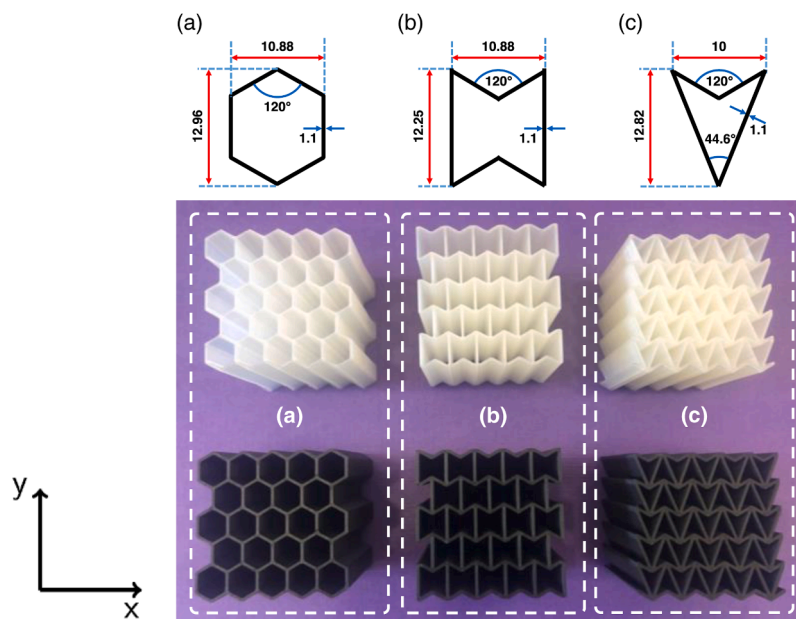


Fig. 2. Unit cell topologies and 3D printed cellular structures for the (a) hexagonal, (b) re-entrant and (c) double arrowhead designs shown in Nylon (white material) and Onyx (black material) (units in mm).

Table 1
Compressive mechanical properties of Nylon and Onyx 3D printed samples.

Material	Young's Modulus (GPa)	Poisson's Ratio	Yield Stress, σ_y (MPa)	Density [31] (kg/m^3)
Nylon	0.826	0.432	31.451	1100
Onyx	1.392	0.379	40.520	1180

3. Experimental testing and data reduction

3.1. Material characterisation

Appropriate material characterisation was conducted to obtain the necessary properties for computational analysis. Isotropic elastic-plastic material properties of 3D printed material may be approximated by printing samples with a +/- 45° orientation angle [29]. Therefore, Nylon and Onyx characterisation samples were printed with alternating layers of +/- 45° print orientation according to the ASTM D695 standard [30]. All testing was conducted using a Zwick Z100 Universal Test Machine with a 100 kN load cell. Compression tests were conducted at a constant rate of 5 mm/min. La Vision 2D Digital Image Correlation (DIC) software was used to track deformation and therefore strain, during each uniaxial compression test. The corresponding material properties were calculated from the obtained stress – strain curves and are presented in Table 1.

3.2. Quasi-static compression testing

Quasi-static compression tests on the 3D printed composite samples were carried out using an Instron 4045 Universal Test Machine. The 50×50×50 mm³ samples were placed between two stainless steel platens and subjected to loading at a crosshead displacement rate of 10 mm/min. The load – displacement traces were recorded to obtain compressive strength and energy absorption characteristics of the core structures. The structures were tested under two uniaxial loading directions, as shown in Fig. 3, as both loading directions of the re-entrant structure produce an auxetic response. The double arrowhead is primarily reported to be auxetic in one direction (in-plane) however these samples have also been tested in the axial direction for completion. These directions are referred to as IP (in-plane) and AX (axial) respectively and correspond with the y and x direction respectively, as shown in Fig. 3.

Table 2 summaries the test plan for experimental compression.

3.3. Data reduction

During compression, each structure is expected to experience three distinct phases: linear elastic deformation, followed by a plateau phase of plastic deformation and densification. Following quasi-static compression, the following parameters are calculated to compare the energy absorbing behaviour of the tested structures and orientations.

3.3.1. First maximum compressive strength

The first maximum compressive strength corresponds to first local maximum compressive stress within the stress – strain curve and signals the onset of plastic deformation. However, not all structures exhibit this peak and instead, the stress rises steadily towards final densification.

3.3.2. Plateau stress

Following linear elastic deformation, continual application of compressive force sees each sample deform plastically, exhibiting a plateau phase on the stress – strain curve before final densification. The plateau stress describes the numerical mean value of stress experienced by the structure during the 20 and 30% compressive strain.

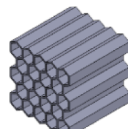
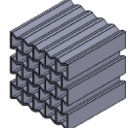
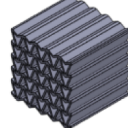
3.3.3. Energy Absorbed (EA) (up to 50% strain)

The energy absorbed up to 50% strain is the integral of the force – displacement curve up to a crosshead displacement, d, of 25 mm, Eq. (1):

$$EA = \int_0^d F(y)dy \tag{1}$$

where F is the compressive force and y is the instantaneous displacement of the crosshead.

Table 2
Tested samples for quasi-static compression testing.

Structure	Material	Loading Direction	Sample ID
	Nylon	In-plane	HEX_N_IP
		Axial	HEX_N_AX
	Onyx	In-plane	HEX_O_IP
		Axial	HEX_O_AX
	Nylon	In-plane	REE_N_IP
		Axial	REE_N_AX
	Onyx	In-plane	REE_O_IP
		Axial	REE_O_AX
	Nylon	In-plane	DAH_N_IP
		Axial	DAH_N_AX
	Onyx	In-plane	DAH_O_IP
		Axial	DAH_O_AX

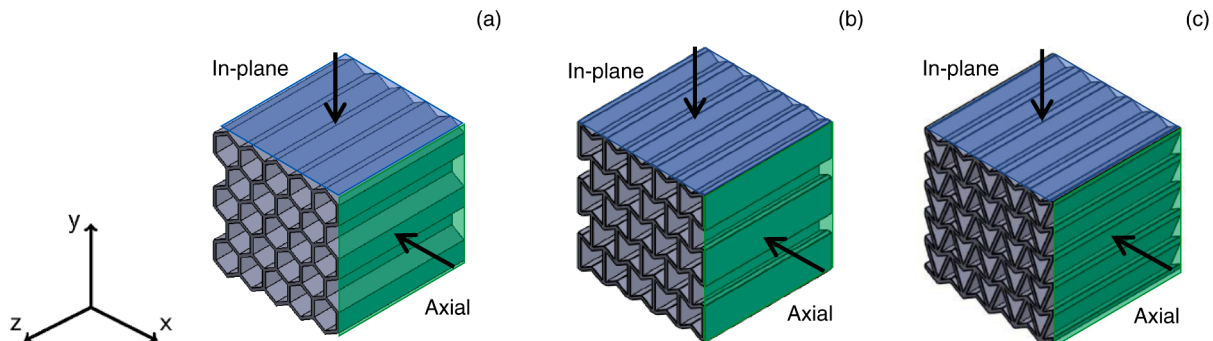


Fig. 3. Experimental loading in the in-plane (IP) and axial (AX) directions for the (a) hexagonal, (b) re-entrant and (c) double arrowhead structures.

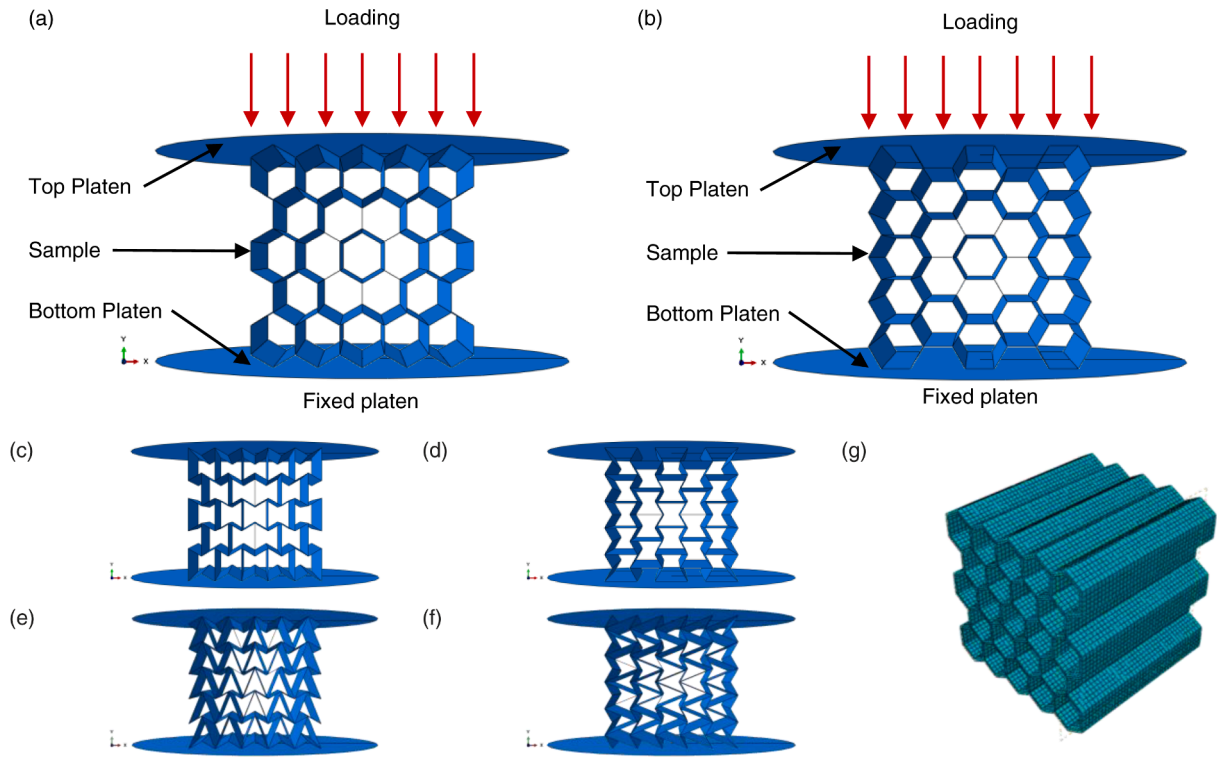


Fig. 4. Loading and boundary conditions on cellular structures modelled using FE software Abaqus/CAE® 2017: hexagonal samples in the (a) in-plane and (b) axial loading directions; re-entrant samples in the (c) in-plane and (d) axial loading directions; and double arrowhead samples in the (e) in-plane and (f) axial loading directions. Shells were meshed using S4R elements as shown for the (g) HEX_O_IP model.

3.3.4. Specific Energy Absorbed (SEA)

Given the different topologies tested and materials used, the various structures possess different masses. Therefore, specific energy absorption is an important parameter when comparing compressive behaviour and is calculated using Eq. (2) to ascertain the EA per unit mass. A high SEA indicates greater energy absorption per unit mass. Again, this indicator has been calculated up to 50% compressive strain ($d = 25$ mm) in accordance with the ISO 13314 [32].

$$SEA = \frac{\int_0^d F(y)dy}{m} \tag{2}$$

where m is the mass of the tested sample.

4. Numerical modelling

4.1. Finite element modelling

Quasi-static compression was modelled using commercial FE software Abaqus/CAE® 2017 [33]. Compression samples were modelled as

3D deformable extruded shells, as presented in Fig. 4. The material properties presented in Table 1 are used for the Nylon and Onyx samples. The compression platens were modelled as two analytical rigid surfaces. The lower platen was fixed, whereas the upper platen was permitted to move in the negative y -direction up to the maximum displacement achieved during the experiment, to allow for compression simulation. A coefficient of friction of 0.2 was applied between the platens and sample [15]. To investigate the two loading directions, the models were orientated accordingly, as shown in Fig. 4. Mesh convergence was conducted and as the structures were composed of extruded shells, a global seed size and sweeping mesh of S4R elements were applied, as shown in Fig. 4 (g).

4.2. Variable cell wall thickness

When designing each cellular structure, a cell wall thickness of 1.1 mm was selected to satisfy printing parameters. However, with FFM a common drawback is the lack of dimensional accuracy due to temperature variations across the print bed during printing. For complex builds, different areas of the part may cool faster than others and result in

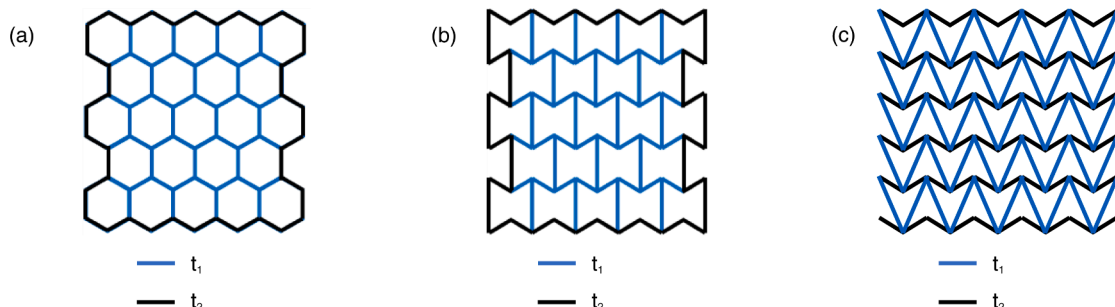


Fig. 5. Wall thickness variations (as presented in Table 3) for (a) hexagonal, (b) re-entrant and (c) double arrowhead samples.

Table 3
Applied thickness values for computational model (in mm).

Sample ID	t_1	t_2
HEX_N_IP	0.70	0.91
HEX_N_AX	0.71	0.91
HEX_O_IP	1.02	1.09
HEX_O_AX	1.02	1.09
REE_N_IP	0.72	0.73
REE_N_AX	0.75	0.78
REE_O_IP	1.07	1.06
REE_O_AX	1.08	1.08
DAH_N_IP	0.73	0.80
DAH_N_AX	0.68	0.93
DAH_O_IP	0.97	1.27
DAH_O_AX	0.95	1.26

shrinkage or warpage. As a result, the average cell wall thickness was measured following printing and samples have been separated into two distinct printing regions, t_1 and t_2 , as shown in Fig. 5 (with the corresponding dimensions recorded in Table 3). In order to better replicate the printed structures, cell wall thicknesses have been separated into inner and outer cell walls for the hexagonal and re-entrant samples and long and short cell walls for the double arrowhead samples. With Nylon, there was pronounced shrinkage experienced and the printed cell wall thickness was lower than the designed thickness. With Onyx, cell wall thickness measurements were found to be geometrically closer to the

designed structures due to the embedded carbon fibre strands.

Within literature, the discrepancy between computational simulation and experimental tests is suggested to be caused by the variation in cell thickness following printing [15]. Fig. 6 compares the experimentally obtained (a) mass and (b) plateau stress with the FE simulation using a uniform cell wall thickness of 1.1 mm and the variable thickness approach described above. As presented, this variable thickness method allows for an accurate assessment of the structural mass and compressive plateau stress experienced.

4.3. Theoretical approximation of plastic collapse stress

The hexagonal honeycomb investigated within this study behaves as an elastic-plastic solid. Following the application of a compressive load the cell walls begin to bend until collapse. Here, the elastic yield point is reached and plastic hinges form within the structure. This corresponds to the plastic collapse stress, σ_{pl}^* and the formation of the plateau region within the stress – strain curve. Fig. 7 (a) presents the loading of the honeycomb in the in-plane direction. The derived form of the plastic collapse stress within this loading direction is given by Eq. (3) [1]. Axial loading is shown in Fig. 7 (b) and is represented by Eq. (4) [1]. The values of cell wall thickness, t , cell wall lengths, h and l , and cell angle, θ , correspond to the geometric properties in Fig. 7.

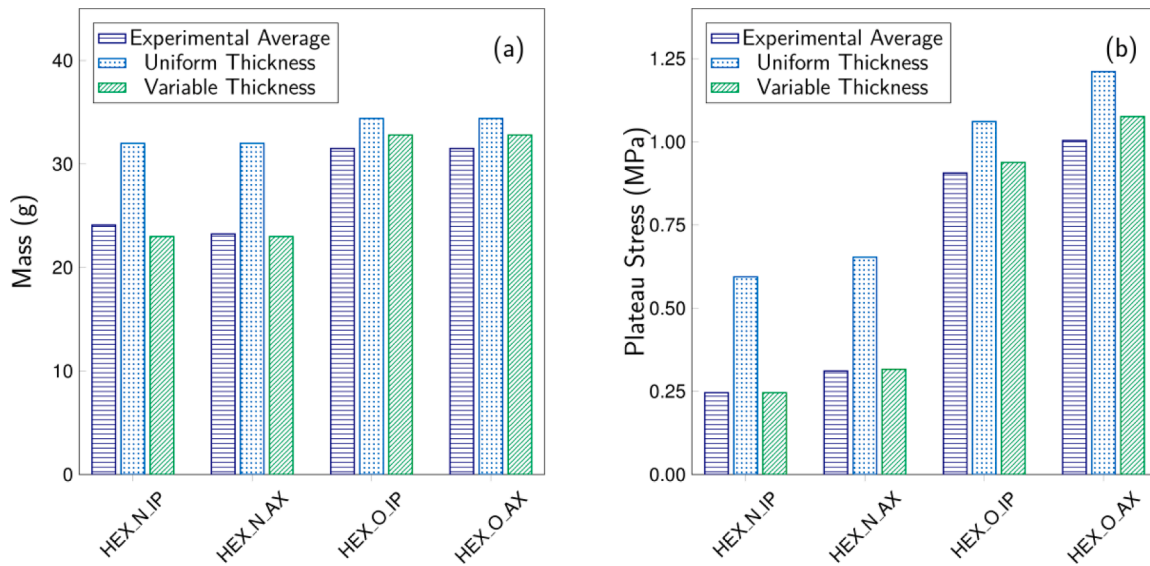


Fig. 6. Comparison of experimental properties with computational uniform or segregated variable thicknesses for (a) mass (in grams) and (b) plateau stress (in MPa).

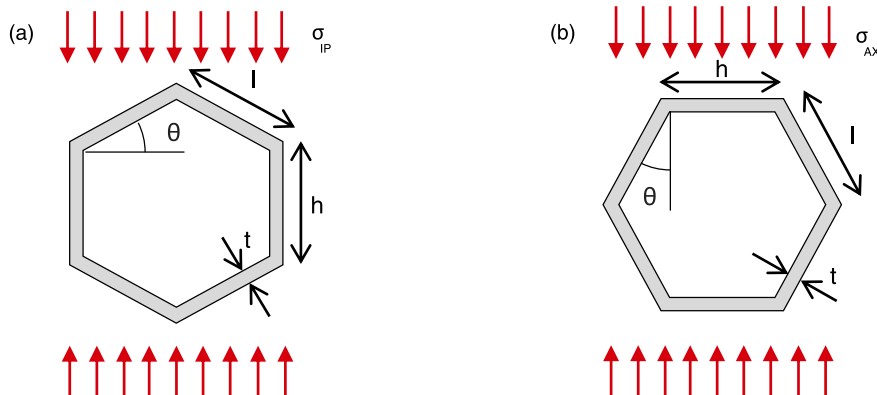


Fig. 7. Schematic of the hexagonal model under (a) in-plane and (b) axial loading.

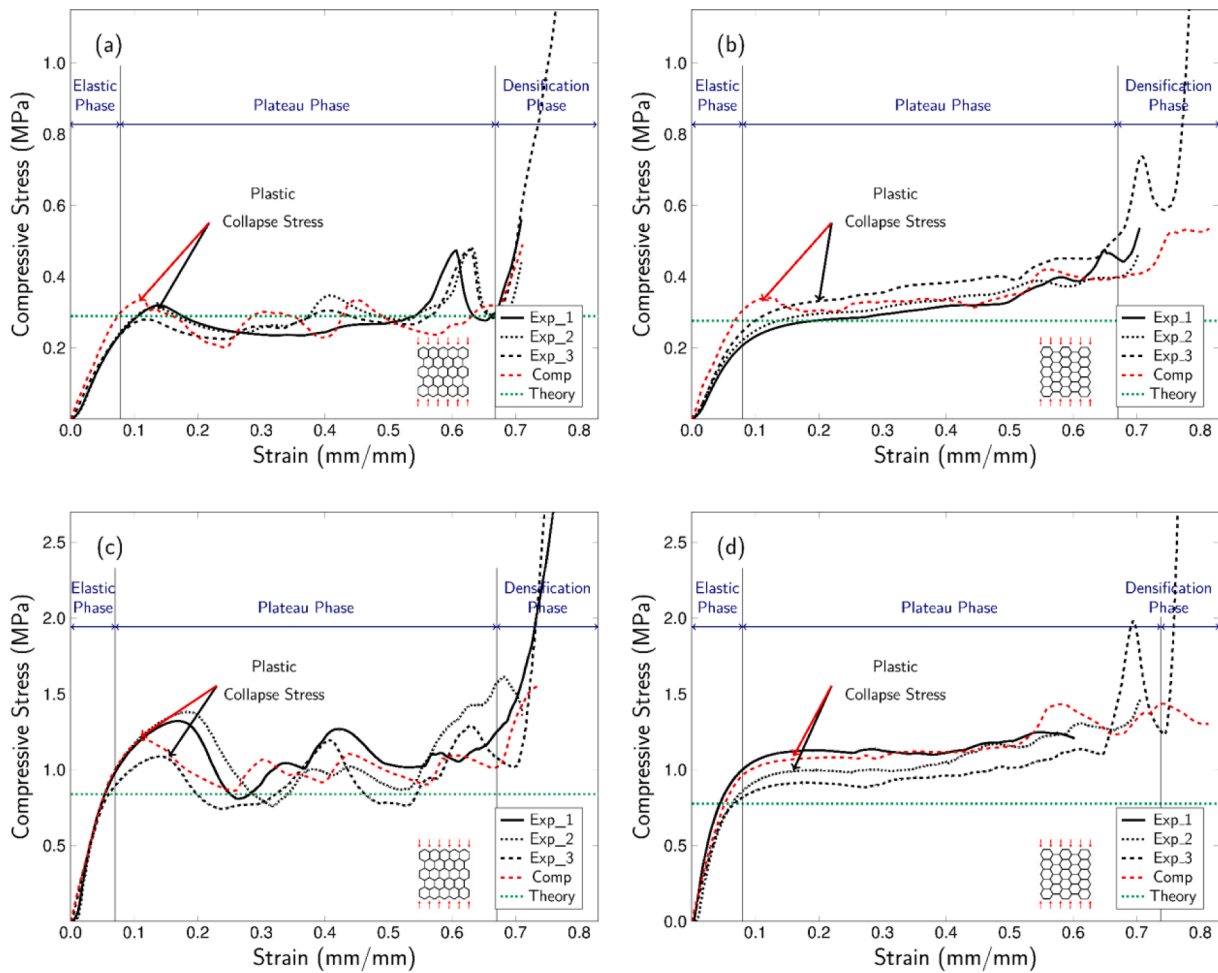


Fig. 8. Compressive stress – strain curves for hexagonal models comparing the experimental, computational and theoretical approximations: (a) HEX_N_IP, (b) HEX_N_AX, (c) HEX_O_IP and (d) HEX_O_AX.

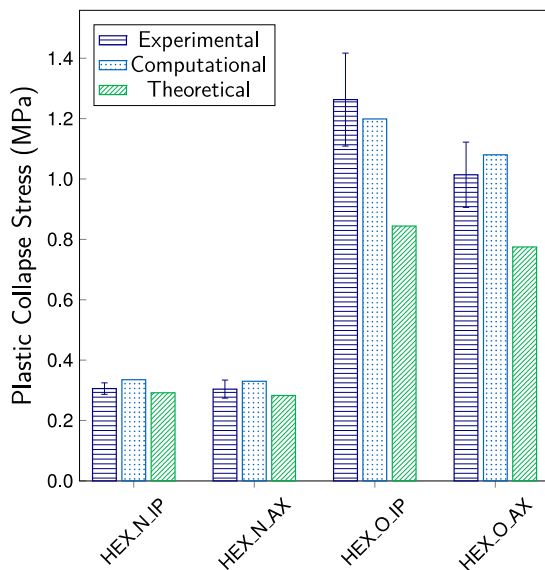


Fig. 9. Comparison of experimental, computational and theoretical approximations of plastic collapse stress (in MPa) for the hexagonal structures.

$$\frac{(\sigma_{pl}^*)_{IP}}{\sigma_{ys}} = \left(\frac{t}{l}\right)^2 \frac{1}{2\cos^2\theta} \quad (3)$$

$$\frac{(\sigma_{pl}^*)_{AX}}{\sigma_{ys}} = \left(\frac{t}{l}\right)^2 \frac{1}{2(h/l + \sin\theta)\sin\theta} \quad (4)$$

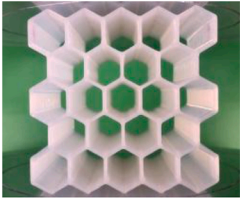
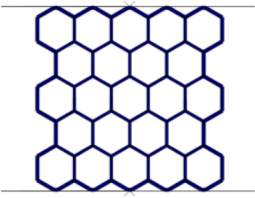
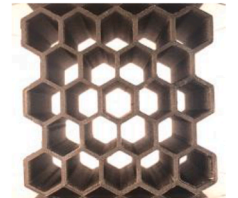
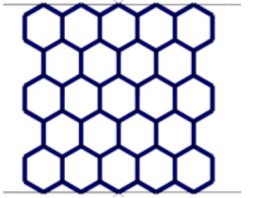
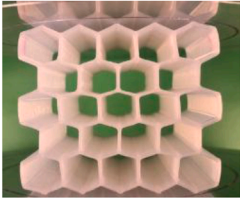
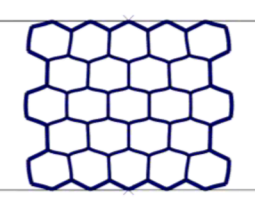
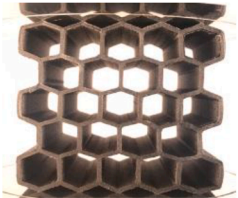
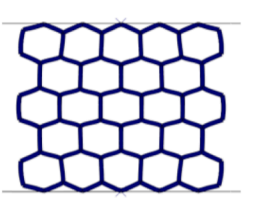
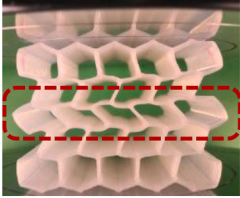
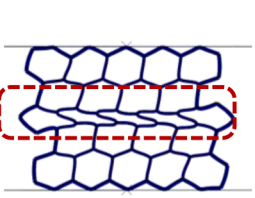
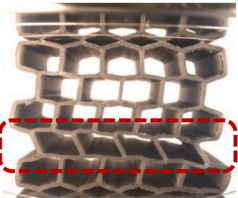
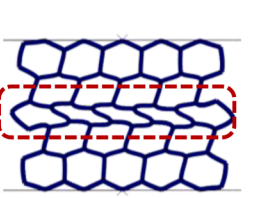
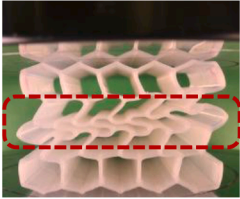
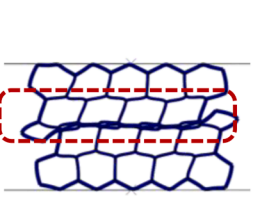
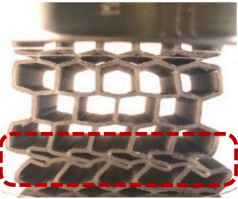
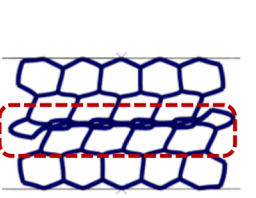
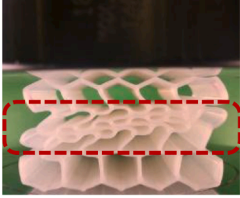
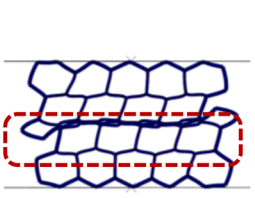

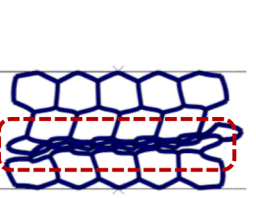
5. Results and discussion

5.1. Numerical and experimental loading response

The FE models of each hexagonal sample have been compared with experimental test data and the theoretical approximation for plastic collapse stress. The compressive stress – strain curves for the Nylon and Onyx Hexagonal models, loaded in-plane ((a) and (c)) and axially ((b) and (d)), are presented in Fig. 8. The computational simulations were capable of providing an accurate representation of the stress – strain curvature, identifying correctly the three distinct phases observed. Linear elasticity is observed before plastic deformation occurs at the plastic collapse stress; a plateau region follows, and plastic deformation continues as each layer of cells buckle and collapse before final densification is achieved.

Firstly, by introducing a compression load, the structures begin to elastically deform through bending dominated behaviour. Within this region, the stress – strain curve rises linearly until the point at which plastic hinges are formed. Here the curves enter their plateau phase which is characteristically different depending on the loading direction.

Table 4
Experimental and computational deformation for the HEX_N_IP and HEX_O_IP models under compression.

Disp. (mm)	Nylon		Onyx	
	Experimental	Computational	Experimental	Computational
0				
5				
10				
15				
20				

For structures loaded in-plane, the force is applied to cell walls which are orientated parallel to loading. Therefore, the cell walls bend until buckling occurs which corresponds to the rise and fall of stress as shown in Fig. 8 (a) and (c). However, when axially loaded the force is applied to cell walls which are perpendicularly orientated before being transferred to the diagonal cell walls. As a result, the bending occurs at the hinge location forcing the diagonal cell walls to simply flatten. This corresponds to a steady and gradual rise of stress within the plateau phases in Fig. 8 (b) and (d). The plastic deformation of both loading orientations continues with the sequential buckling of each layer of cells before the final phase occurs. The densification phase is characterised by a sharp rise in stress as all voids within the structure are filled.

A comparison of the experimental, computational and theoretical approximation for plastic plateau stress is presented in Fig. 9. Through theoretical approximation, it is possible to predict the plastic collapse stress accurately for the models composed of Nylon (HEX_N_IP and HEX_N_AX). However, the theoretical approximation for the Onyx samples (HEX_O_IP and HEX_O_AX) experiences a greater discrepancy between the computational and experimental values. The theoretical approximation is derived from one single unit cell rather than an interconnected stacked cellular structure. Therefore, this approximation does not incorporate the additional reinforcement provided by the

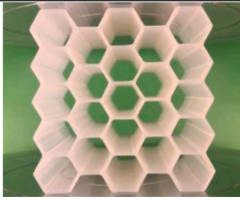
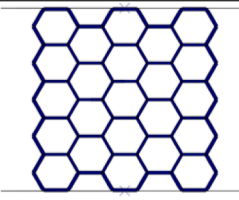
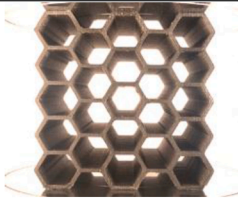
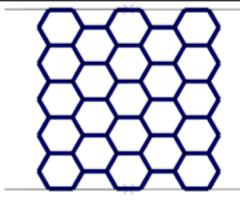
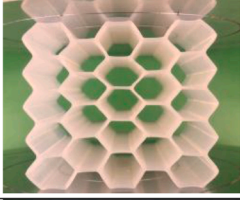
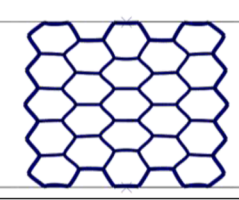

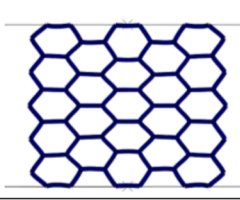
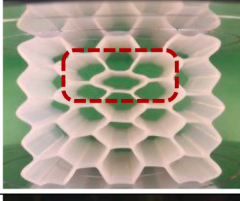
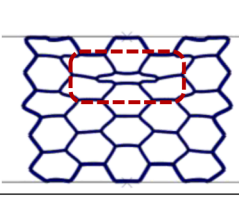
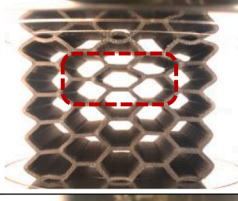
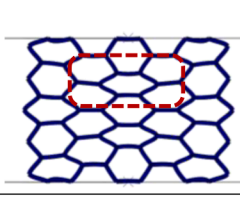
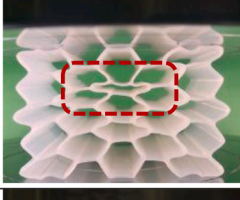
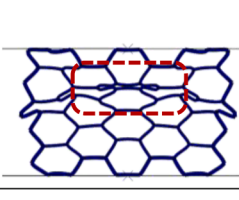
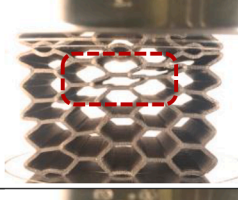
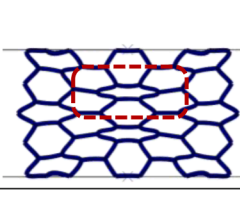
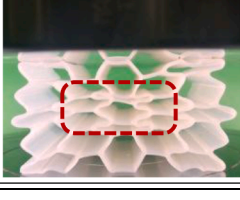
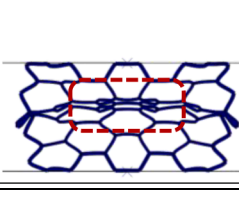
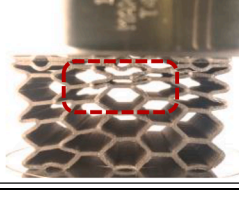
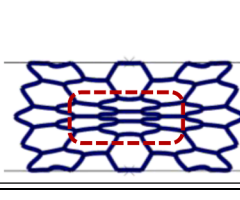
surrounding cells. The samples composed of Onyx material require a larger compressive stress to yield and begin plastic deformation. This is due to the additional stiffness provided from the chopped carbon fibres which are not present in conventional Nylon. However, each of the computational models have been validated using the experimental results obtained.

5.2. Modes of deformation

5.2.1. Hexagonal (non-auxetic) structures

The deformation patterns for the hexagonal models are presented in Tables 4 and 5 for the in-plane and axially loaded structures respectively. As presented, the computational simulation is capable of predicting similar deformation modes to those observed throughout each experiment. When loaded in-plane, deformation occurs as the central row of cells folds and subsequently causes an adjoining row to fail. For the structures which are axially loaded, it becomes apparent that the structures' diagonal cell walls bend, flattening the centrally located unit cells, as indicated. This is characteristic of non-auxetics where structures will move away from the applied loading direction, expanding perpendicularly. When comparing the two orientations investigated, there are distinct similarities in the overall shape of the stress – strain curves

Table 5
Experimental and computational deformation for the HEX_N_AX and HEX_O_AX models under compression.

Disp. (mm)	Nylon		Onyx	
	Experimental	Computational	Experimental	Computational
0				
5				
10				
15				
20				

presented in Fig. 8. Additionally, with the visual agreement between the computational and experimental structures (Tables 4 and 5), the deformation modes occur irrespective of the material and are dependent upon loading direction. By altering the loading direction, the structures behave as unique structures with differing deformation modes dictating their compressive behaviour.

5.2.2. *Re-entrant (auxetic) structures*

The force – displacement curves, obtained from the experimental test machine for the Nylon and Onyx re-entrant models and the simulation loaded in-plane ((a) and (c)) and axially ((b) and (d)), are presented in Fig. 10. For the REE_N_AX and REE_O_AX, the results of only one and two samples are presented, respectively, due to the premature failure of the other samples during testing. Additionally, the experimental and computational deformation patterns obtained at 5 mm displacement increments are presented. As was observed with the hexagonal models, the re-entrant models exhibit different behaviour depending upon the loading orientation and more details may be found in Appendix A.

Again, three main phases may be observed during the compression of each re-entrant structure. When loaded in-plane, the curve exhibits a sharp rise as the first peak forms. Following this the first row of cells buckles and the force drops. The plateau region which then occurs sees each layer of cells fold sequentially with a corresponding peak forming

for each fold. Final densification is achieved as the folded layers come into contact and the force rises. For the axially loaded structures, the force – displacement curves for both Nylon and Onyx materials are characterised by an initial linear response, followed by one distinct peak forming. Following this, the force reduces, and the curve enters the plateau phase. During this phase, the diagonal cell walls fold and form a “V-shaped” concentrations, as presented in Fig. 11. These concentrations form as the diagonal cell walls buckle and are restricted between the horizontal cell walls located above and below. These formations signify an overall global instability of the structure as it bulges outward. Therefore, these samples no longer experience an auxetic effect. Final densification occurs as all the cell walls come into contact and corresponds with a gradual increase in the force experienced.

5.2.3. *Double arrowhead (auxetic) structures*

The experimental and computational force – displacement curves obtained for the Nylon and Onyx double arrowhead models, loaded in-plane ((a) and (c)) and axially ((b) and (d)), are presented in Fig. 12. The deformation patterns at 5 mm increments are also compared (and fully presented in **Error! Reference source not found.**).

As presented, when loaded in-plane the double arrowhead structures experience elastic deformation as the cell walls begin to bend and deform. Following the peak force, it is possible to observe the auxetic

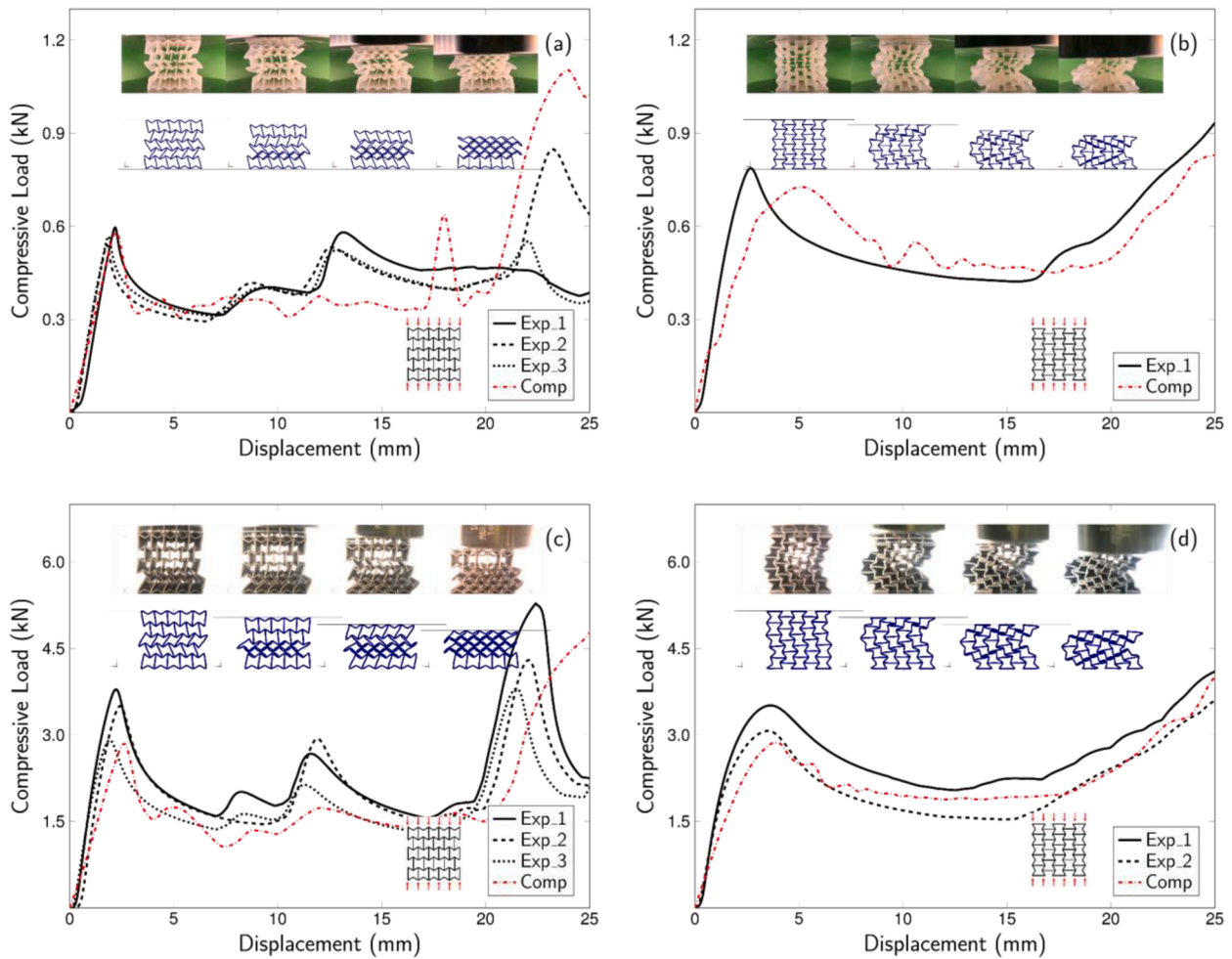


Fig. 10. Compressive load – displacement curves for the re-entrant models: (a) REE_N_IP, (b) REE_N_AX, (c) REE_O_IP and (d) REE_O_AX.

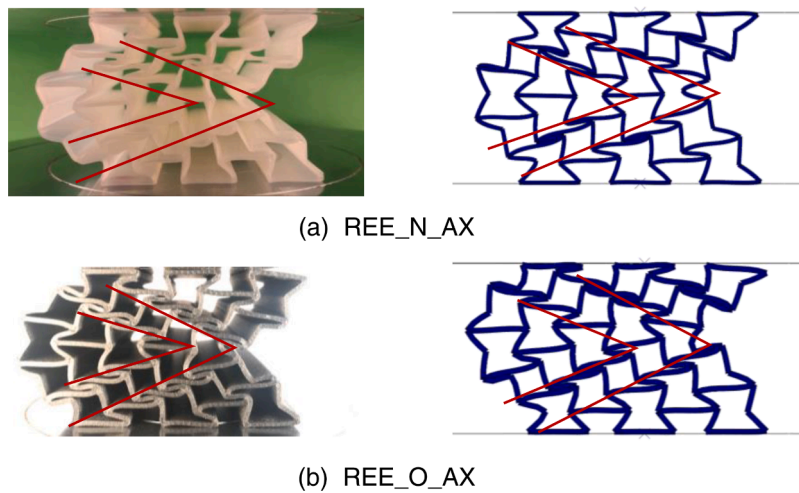


Fig. 11. Deformation of (a) REE_N_AX and (b) REE_O_AX at 15 mm displacement with formation of “V-shaped” concentrations.

effect of internal densification under the applied loading, as shown in Fig. 13 (at 5 mm displacement). For the (a) Nylon structure, the auxetic effect is observed by the internal densification of the top-right and bottom-left cells which begin compressing. Within the (b) Onyx structure the bottom row of cells deform under this applied compression causing internal densification. These initial weaknesses provide a

deformation path which then begin to impact surrounding cells. By 15 mm displacement, the central row of cells collapses, and final densification of the structure occurs. Favourably, following the initial peak force there is only a small reduction in force before it begins to rise steadily.

When loaded axially, the double arrowhead structures behave as an

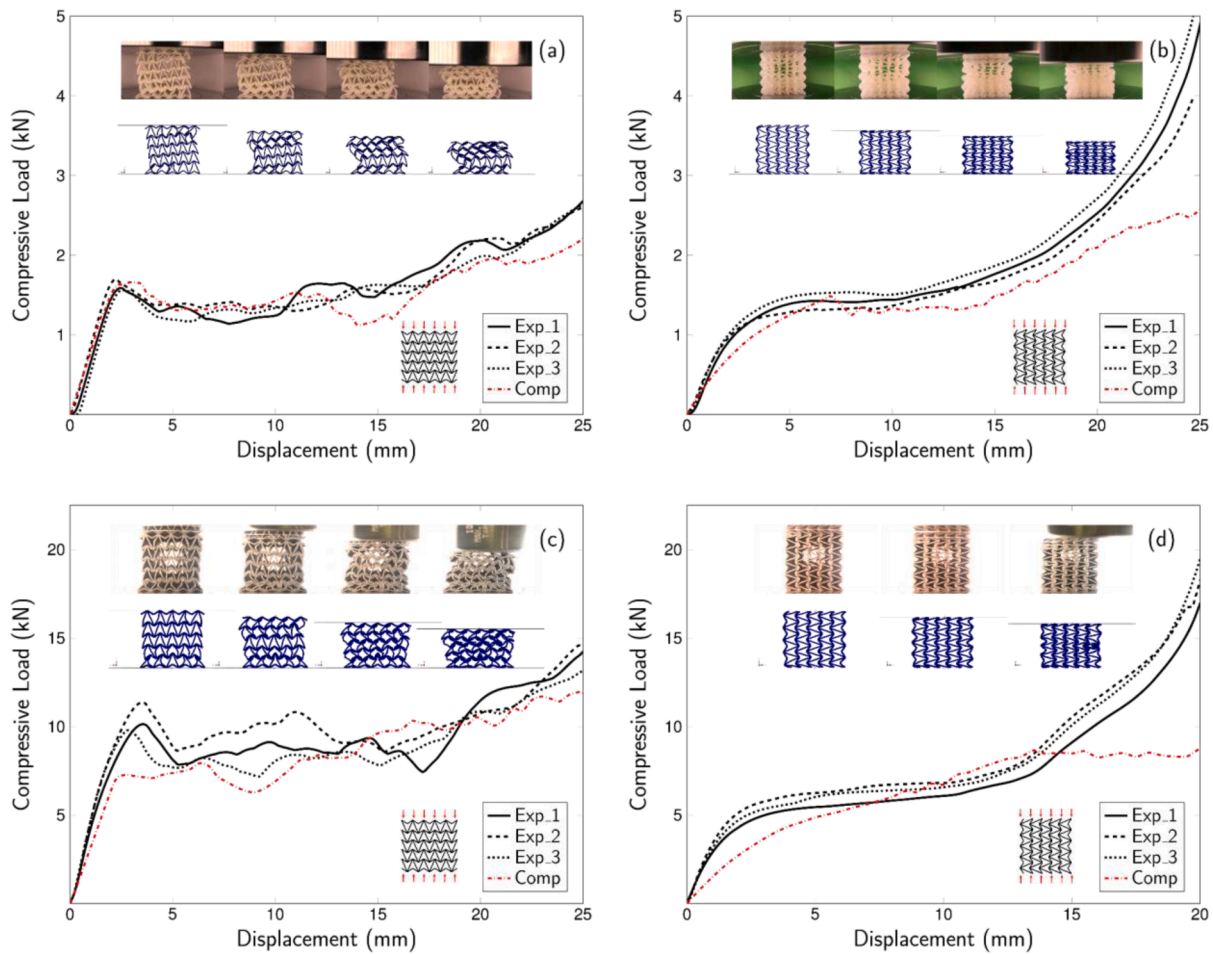


Fig. 12. Compressive force – displacement curves for the double arrowhead models: (a) DAH_N_IP, (b) DAH_N_AX, (c) DAH_O_IP and (d) DAH_O_AX.

auxetic structure and contract inwards as the cell walls fold. As was observed with the hexagonal structures, there is no apparent peak force formed with the double arrowhead structures. This is due to the direction the load is transferred throughout the structure. The double arrowhead shape allows for an easy transfer of load throughout the structure as the crosshead displacement increases. For the Onyx structure, final densification occurs much sooner than the Nylon counterpart and as a result, force – displacement is only recorded up to 20 mm crosshead displacement.

Notably, a discrepancy is observed between the computational simulation and experimentally tested structures within the final densification phase of the axially loaded samples. This is caused by an inability to accurately model the “pointed” region of the double arrowhead unit cell. The shell models which were used within the simulations have a section thickness applied offset from the middle surface, Fig. 14 (a). Final densification occurs as these pointed regions are compressed and fold, and are therefore in contact with each other, as shown in Fig. 14 (b) and (c). The folding of these pointed regions is not effectively modelled until a greater crosshead displacement is achieved, hence causing this discrepancy. The plateau region and overall curve shape have however been accurately modelled.

From the presented force – displacement curves it has been observed how each structure reacts differently under compressive loading depending on their loading orientation, irrespective of the material selected. The auxetic nature has been shown by the (in-plane) re-entrant and the double arrowhead unit cells which internally densify initially under compression. Whereas, the hexagonal structures presented typical non-auxetic behaviour. A comparison of the compressive structural

properties and material selection will be discussed in the next section.

5.3. Compressive material properties and energy absorption

The compressive properties obtained experimentally and computationally through the FE simulation are presented in Table 6.

5.3.1. First maximum compressive strength

The results obtained for first maximum compressive failure are presented in Fig. 15 (a) and (b) for the Nylon and Onyx structures respectively. As observed from the stress – strain curves and force – displacement curves, not all structures experience an initial local maximum and therefore, for these structures the first compressive strength cannot be determined. The first maximum compressive strength occurs at the initial peak point on the force – displacement curves before a noticeable drop in force is experienced. Therefore, the following structures did not experience any initial peak formation: HEX_N_AX, HEX_O_AX, DAH_N_AX and DAH_O_AX. As presented, there remains good agreement between the experimentally obtained average and computational simulation.

Fig. 16 presents the loading scenario and deformation experienced by each unit cell structure. For the (a) hexagonal and (c) re-entrant samples orientated in-plane, load is transferred through the vertical members which run parallel to the loading direction. This load is then transferred to the adjoining diagonal cell walls. Buckling of the vertical members occurs when the compressive force exceeds the Euler buckling load and causes the wall to rotate, as shown by the angle of rotation, ϕ , in Fig. 16. Bending occurs within the diagonal cell walls as a result of the

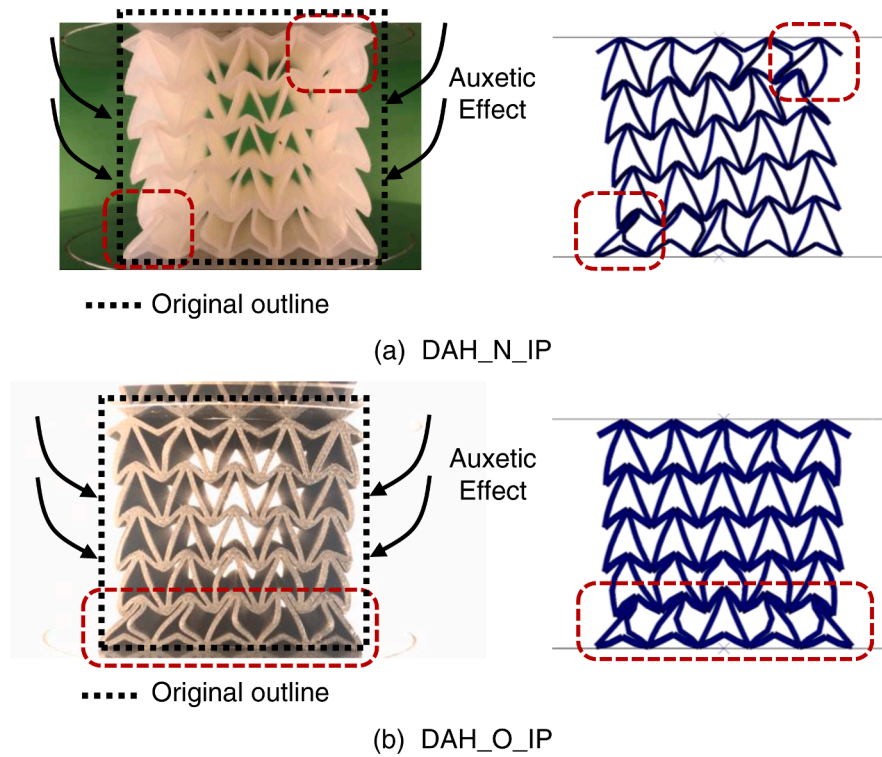


Fig. 13. Deformation of (a) DAH_N_IP and (b) DAH_O_IP at 5 mm displacement with internal densification or “auxetic” effect

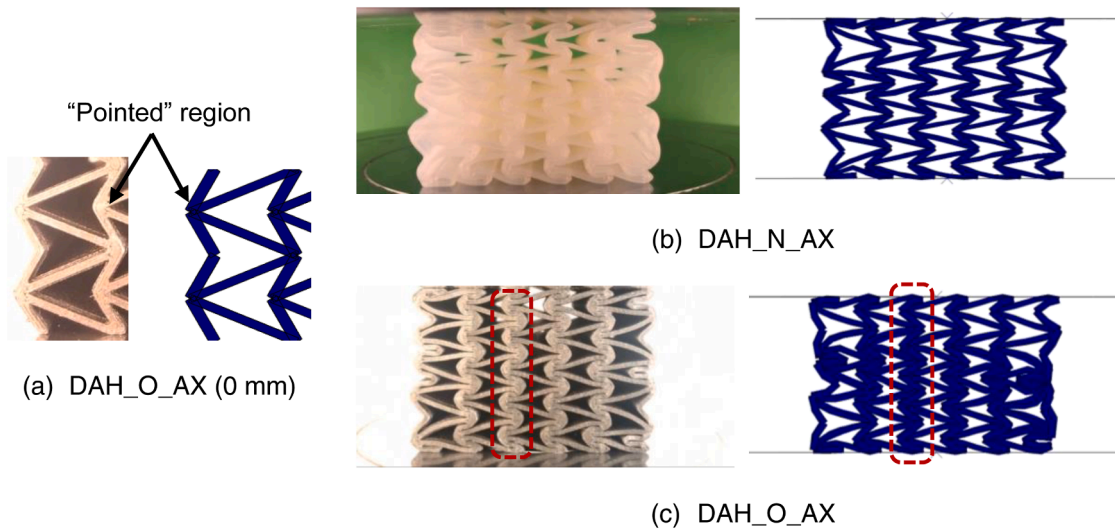


Fig. 14. Double arrowhead samples loaded in the axial direction: (a) discrepancy caused by modelling of double arrowhead geometry; (b) DAH_N_AX and (c) DAH_O_AX at 20 mm displacement with internal densification.

moments experienced causing collapse of the unit cell and a notable peak within the stress – strain curve.

When loaded axially, the (b) hexagonal and (d) re-entrant samples should effectively flatten as load is transferred perpendicularly to the horizontal cell wall. The load is then transferred to the diagonal cell walls which bend causing the cells to collapse and flatten. However, there is no sudden buckle as experienced in-plane and no peak force is experienced within the stress – strain curve. The re-entrant samples initially behave this way and begin to fold, as presented in Appendix A up to 5 mm. Following this, the sample deformation is governed by an overall global instability.

When loaded (e) in-plane, the double arrowhead cell walls will bend

before buckling, causing a corresponding peak. However, when (f) axially loaded, plastic hinges located at cell vertices cause a controlled folding of the cell walls and the force – displacement curve forms the plateau region.

When considering the Nylon samples, the HEX_N_IP, REE_N_IP and REE_N_AX structures provide fairly comparable compressive strengths of 0.304 MPa, 0.228 MPa and 0.317 MPa respectively. The same trend was observed for Onyx samples where the HEX_O_IP, REE_O_IP and REE_O_AX structures provide compressive strengths of 1.262 MPa, 1.368 MPa and 1.327 MPa respectively. For both materials tested, the double arrowhead structure provides the greatest first maximum compressive strengths of 0.653 MPa and 4.191 MPa for the DAH_N_IP and DAH_O_IP

Table 6
Experimental and computational compressive properties.

Sample ID	First Max. Comp. Strength (MPa)			Plateau Stress (MPa)			Energy Absorbed (J)			Specific Energy Absorbed (kJ/kg)		
	Exp.	Comp.	% Diff.	Exp.	Comp.	% Diff.	Exp.	Comp.	% Diff.	Exp.	Comp.	% Diff.
HEX_N_IP	0.304	0.333	9.4%	0.246	0.246	0.2%	15.370	16.110	4.8%	0.637	0.700	9.9%
HEX_N_AX	-	-	-	0.311	0.316	1.5%	17.780	18.486	4.0%	0.766	0.797	4.1%
HEX_O_IP	1.262	1.196	5.2%	0.906	0.938	3.5%	59.610	59.564	0.1%	1.889	1.816	3.9%
HEX_O_AX	-	-	-	1.004	1.076	7.2%	59.125	62.947	6.5%	1.878	1.919	2.2%
REE_N_IP	0.228	0.233	2.1%	0.186	0.138	25.4%	10.400	11.116	6.9%	0.352	0.404	14.9%
REE_N_AX	0.317	0.290	8.5%	0.176	0.196	11.1%	13.664	13.640	0.2%	0.463	0.470	1.5%
REE_O_IP	1.368	1.136	16.9%	0.822	0.618	24.8%	52.246	48.526	7.1%	1.392	1.116	19.9%
REE_O_AX	1.327	1.142	13.9%	0.747	0.762	2.1%	59.611	56.116	5.9%	1.549	1.275	17.7%
DAH_N_IP	0.653	0.664	1.7%	0.598	0.544	9.0%	39.762	37.688	5.2%	1.045	0.899	13.9%
DAH_N_AX	-	-	-	0.672	0.541	19.5%	46.863	37.961	19.0%	1.244	0.891	28.4%
DAH_O_IP	4.191	3.169	24.4%	3.605	3.278	9.1%	231.781	212.601	8.3%	4.254	3.301	22.4%
DAH_O_AX	-	-	-	3.062	3.186	4.1%	156.332*	126.059	19.4%	2.872*	2.001	30.3%

* EA and SEA to 40% compressive strain due to premature densification.

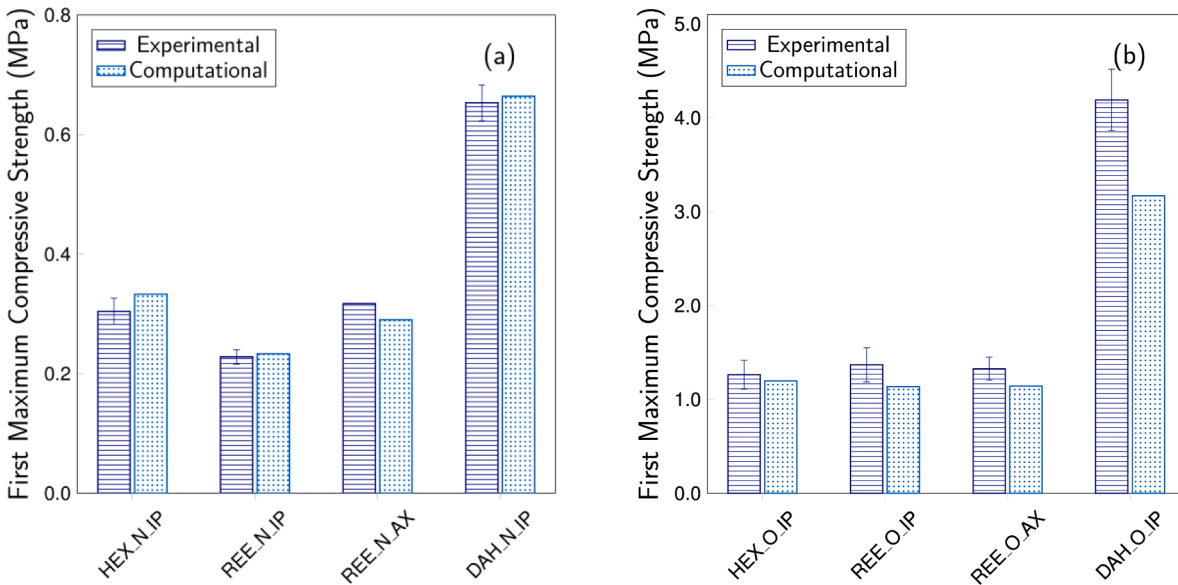


Fig. 15. First maximum compressive strength (in MPa) of (a) Nylon and (b) Onyx models.

structures respectively. The double arrowhead structures (both Nylon and Onyx) were of greater mass than their hexagonal and re-entrant structures and therefore, were able to provide a greater strength under identical loading. However, the significant strength enhancement provided can be attributed to the unique auxetic behaviour experienced rather than just the additional mass within the structure. This will be further analysed by considering the total energy absorbed per unit mass.

5.3.2. Plateau stress

A comparison of experimental and computational plateau stress is presented in Fig. 17 for the (a) hexagonal, (b) re-entrant and (c) double arrowhead structures. As presented for each unit cell, there is a noticeable increase in the plateau stresses obtained by Onyx structures over the conventional Nylon structures. For the hexagonal samples, there was a 268% and 223% change between the Nylon and Onyx structures when loaded in-plane and axially respectively. The lowest plateau stress across all tested models was 0.176 MPa obtained from the REE_N_AX structure. By using Onyx over conventional Nylon, there were 343% and 324% increases for re-entrant models loaded in-plane and axially respectively. Finally, the same trend was observed with double arrowhead structures which saw a 503% and 356% change between the Nylon and Onyx structures with the in-plane and axially loaded models.

The reason that plateau stress was greater for all Onyx loaded

samples is twofold. From Eqs. (3) and (4) it has been shown how the stress within an individual cell is governed by geometric properties of the unit cell (including thickness, t ; height, h ; length, l and angle, θ) and the properties of the base material (yield stress, σ_{ys}). As the Nylon and Onyx structures, all possess identical cell heights, lengths and representative angles, the cell wall thicknesses, and yield stresses are responsible for this improvement in plateau stress. When printed, the Onyx material produces thicker cell walls despite identical slicing parameters. A common drawback of FDM includes shrinkage of materials post-printing. This shrinkage is more prominent with Nylon than Onyx and as a result, yields a thinner cell wall. The chopped reinforcement fibres embedded within Onyx not only reduce shrinkage but improve material properties where yield stress is 40.52 MPa.

5.3.3. Energy absorption and specific energy absorption

The energy absorbed by each of the tested samples up to 50% compressive strain is presented for the (a) in-plane and (b) axial models in Fig. 18. The Onyx samples were capable of absorbing more energy than their Nylon counterparts. This was due to the additional strength provided by the Onyx base material and thicker cell walls as described in the previous section. However, within weight sensitive applications, having a high specific energy absorption is important. The SEA was calculated for each sample and is presented for the (a) Nylon and (b)

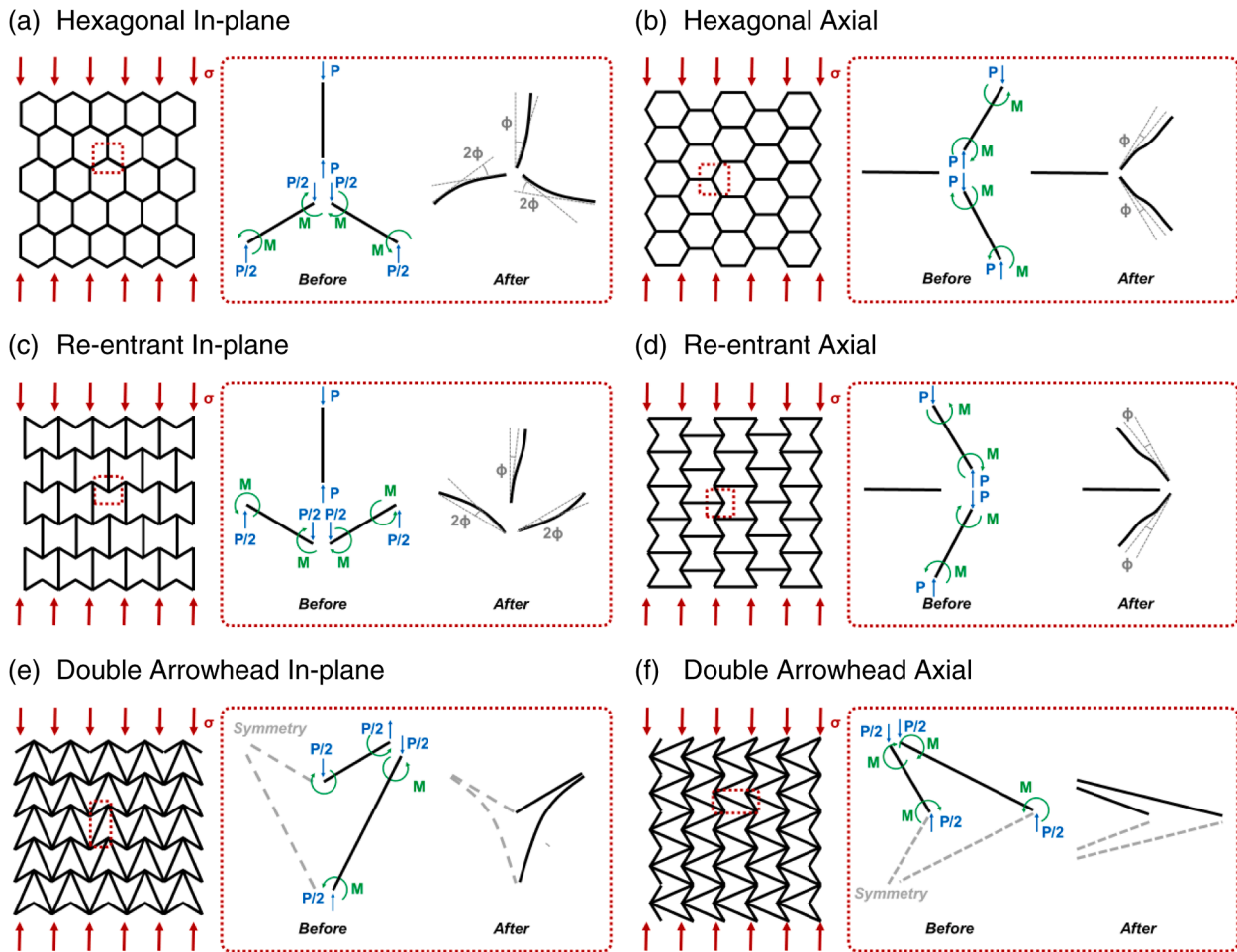


Fig. 16. Failure of individual unit cells under quasi-static compression: (a) hexagonal in-plane, (b) hexagonal axial, (c) re-entrant in-plane, (d) re-entrant axial, (e) double arrowhead in-plane and (f) double arrowhead axial.

Onyx samples in Fig. 19. Good agreement was observed between the experimental tests and computational simulation. The largest discrepancy was observed with the DAH_O_AX model, this primarily being due to the inability to correctly capture the densification phase. Additionally, SEA which is calculated using Eq. (2), includes the accumulated error from EA and the structural mass between the experimental and computational methods.

The geometry associated with the lowest specific energy absorbed by both materials was the re-entrant model loaded in-plane with 0.352 kJ/kg and 1.392 kJ/kg for the Nylon and Onyx samples respectively. Following this, the same auxetic re-entrant unit cell loaded axially, REE_N_AX, absorbed a total of 0.463 kJ/kg. The hexagonal models loaded in-plane and axially, HEX_N_IP and HEX_N_AX, then absorbed 0.637 kJ/kg and 0.766 kJ/kg respectively. The greatest amount of energy was absorbed by the double arrowhead structure. Again, the axial loading direction was deemed superior absorbing 1.244 kJ/kg of energy in comparison to the in-plane loaded configuration which absorbed 1.045 kJ/kg.

For Onyx models, the REE_O_AX, HEX_O_IP and HEX_O_AX models all absorb approximately equal energies of 59.6 J, 59.6 J and 59.1 J respectively. However, as the re-entrant samples are of greater mass than the hexagonal, their SEA is lower. The double arrowhead samples again absorb the greatest amount of energy out of the three different unit cells. However, when loaded axially the samples (DAH_O_AX) absorb less energy than when loaded in-plane (DAH_O_IP). This is due to the fact that the axially loaded model achieved densification much sooner than the other tests (around 20 mm) displacement. Therefore, the total

energy absorbed is only up to 40% compressive strain rather than 50%.

There was a 45% decrease in SEA when comparing the HEX_N_IP and REE_N_IP models. Therefore, the non-auxetic hexagonal structure provided a greater SEA than the auxetic re-entrant. When loaded axially, the re-entrant samples absorbed 40% less than the hexagonal. The same was observed for the Onyx structures where the hexagonal models in both loading directions (HEX_O_IP and HEX_O_AX) provide a greater SEA over the re-entrant models (REE_O_IP and REE_O_AX). This result supports the conclusions presented in [11,15], where re-entrant structures were found to absorb less specific energy than an equivalent hexagonal structure under quasi-static compression.

Despite this, the use of a double arrowhead structure provides superior performance across all materials and loading orientations tested. The greatest SEA of 4.254 kJ/kg was provided by the DAH_O_IP model, a 125% increase over the HEX_O_IP structure. For the Nylon structures, the DAH_N_AX provided the greatest SEA of 1.244 kJ/kg, which is 63% greater than the HEX_N_AX structure. These results highlight the superior specific energy absorbing capabilities of double arrowhead unit cells when compared with a conventional hexagonal and auxetic re-entrant cellular structure. This is due to the internal densification of an auxetic double arrowhead, these cellular structures have been proven to provide superior compressive properties over the other structures tested within this study.

6. Concluding remarks

The compressive properties of three cellular structures (non-auxetic

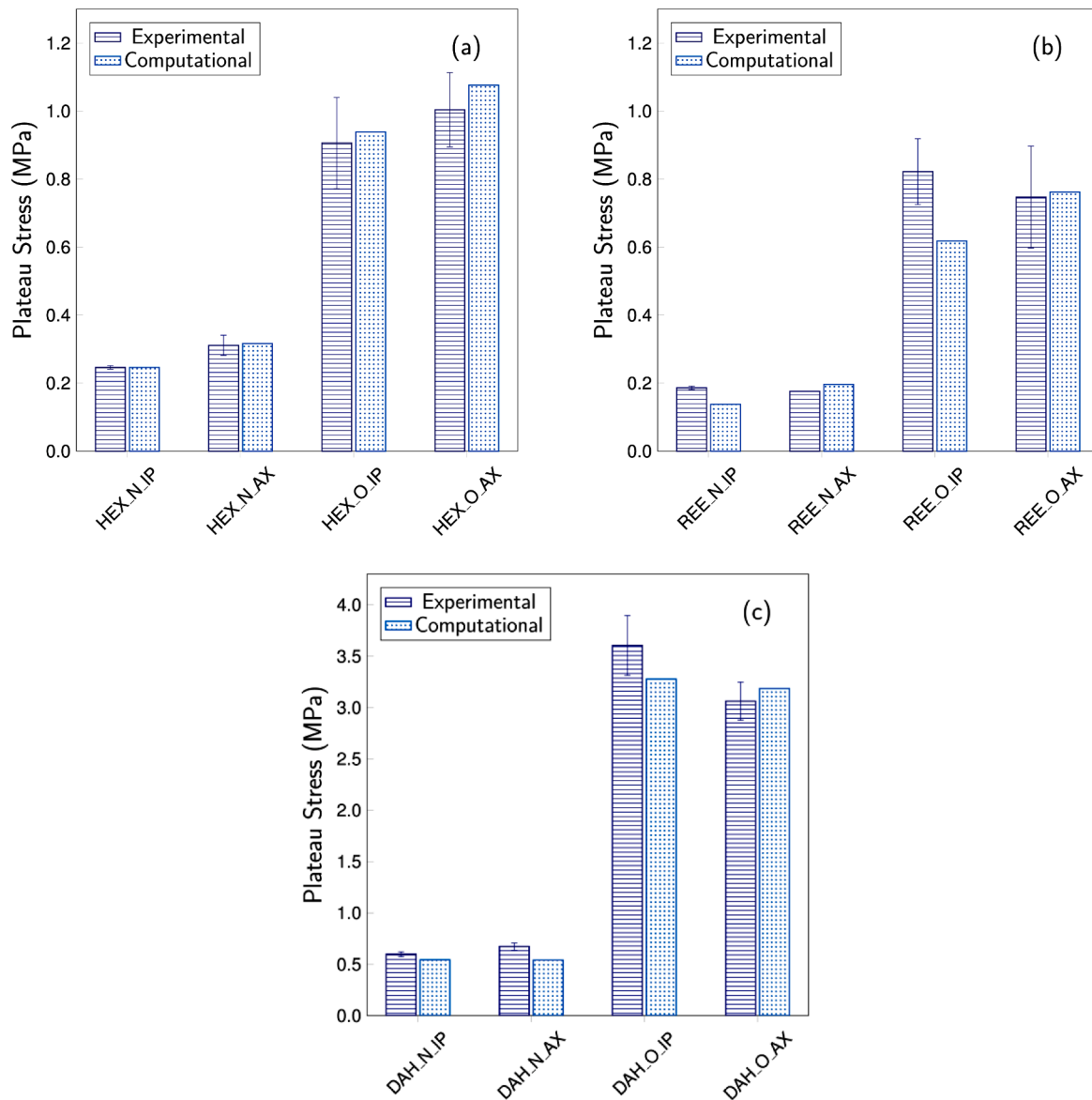


Fig. 17. Plateau stress (in MPa) of (a) hexagonal, (b) re-entrant and (c) double arrowhead models.

hexagonal, auxetic re-entrant and double arrowhead) were studied under two loading orientations and using two different 3D printing materials. The test samples were designed to provide the same number of unit cells per unit area, unit cell thickness, representative angle and overall volumetric dimensions. These samples were manufactured using 3D printing with two materials, a conventional Nylon thermoplastic and a thermoplastic composite (chopped carbon fibre reinforced). A total of 12 different test cases were subjected to quasi-static compression. FE models have been validated using these experimental results and a theoretical approximation for hexagonal honeycombs.

From the results obtained, the following conclusions may be drawn:

- 3D printing results in material shrinkage due to temperature variations during printing. Shrinkage was often greater in the centre of the part. Therefore, variable cell wall thicknesses were considered and applied to the FE simulation accordingly. This helps to obtain a better agreement between the computational and experimental results obtained.
- Of the two materials investigated, composite reinforced material, Onyx, provides superior performance over the unreinforced Nylon material, as expected. Onyx samples for all loading directions and

cellular topologies tested were capable of providing superior compressive strength and specific energy absorption. This is, in part, due to how the material prints through FFM technology and the enhanced material properties of the base material.

- Superior specific energy absorption and compressive strength is provided by the auxetic double arrowhead unit cells, followed by the conventional (non-auxetic) hexagonal and (auxetic) re-entrant unit cells. When loaded in-plane, the composite reinforced thermoplastic double arrowhead unit cells were capable of providing a 125% increase in SEA and 232% increase in compressive strength over the non-auxetic hexagonal. Therefore, auxetic double arrowhead unit cells are capable of providing superior compressive properties over the other cellular structures tested.

Declaration of Competing Interest

The authors declare that they have no known competing financial interests or personal relationships that could have appeared to influence the work reported in this paper.

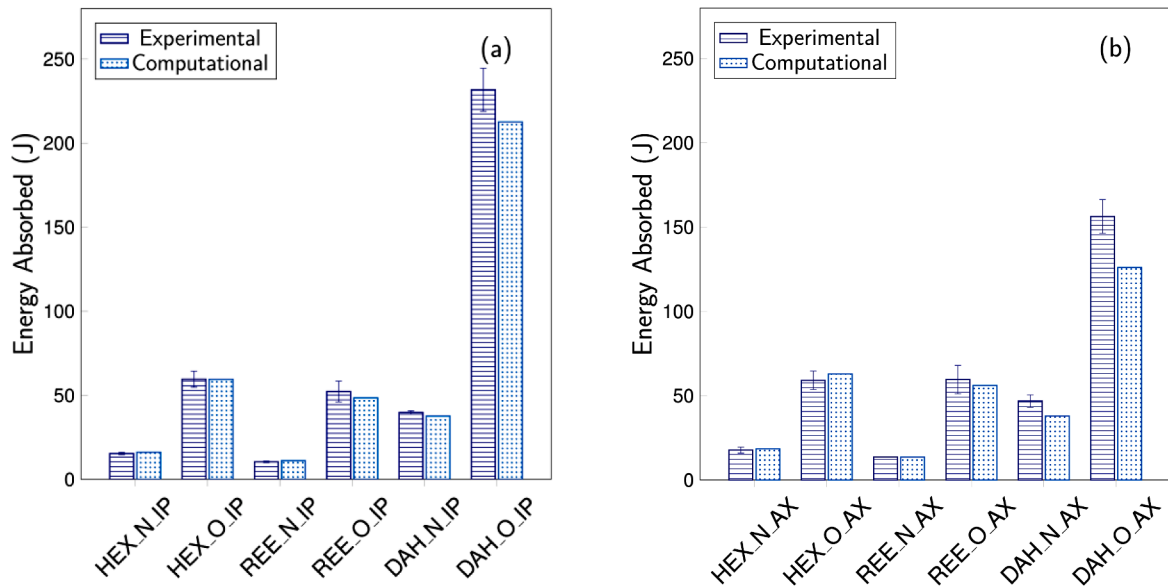


Fig. 18. Energy absorbed up to 50% compressive strain (in J) for the (a) in-plane and (b) axial models.

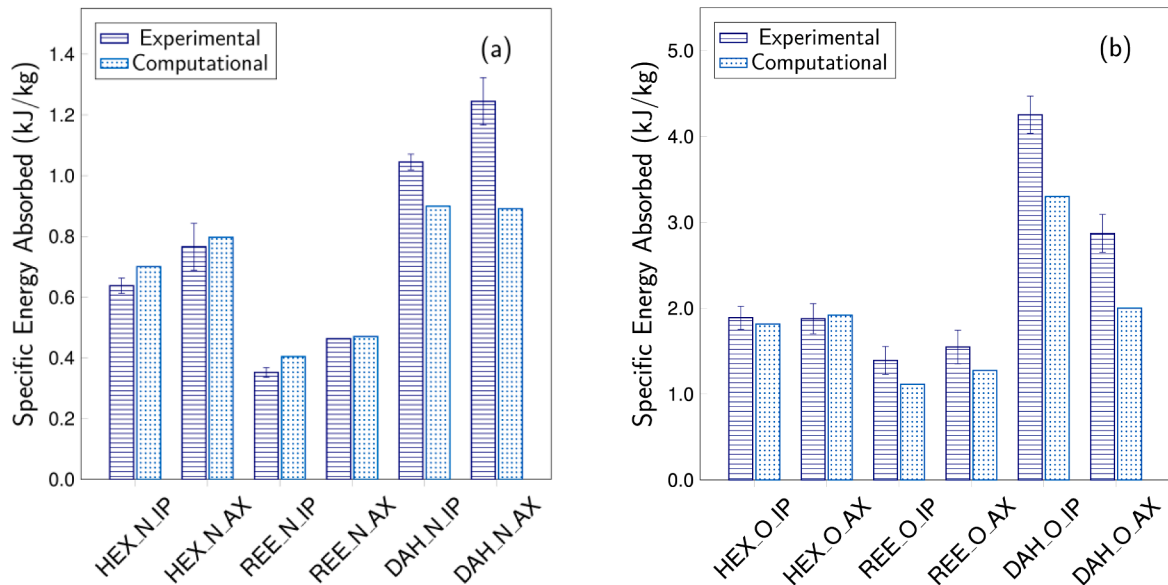


Fig. 19. Specific energy absorbed up to 50% compressive strain (in kJ/kg) for the (a) Nylon and (b) Onyx models.

Data Availability

Data will be made available on request.

Acknowledgements

This research has been kindly funded by the Royal Academy of Engineering Industrial Fellowship Scheme, UK (grant number IFS1819 \40).

Supplementary materials

Supplementary material associated with this article can be found, in the online version, at doi:10.1016/j.ijmecsci.2022.108054.

References

- [1] Gibson LJ, Ashby MF. The mechanics of honeycombs. Cell. Solids Struct. Prop. Cambridge University Press; 1997. p. 93–174. <https://doi.org/10.1017/CBO9781139878326.006>.
- [2] Yang M, Qiao P. Quasi-static crushing behavior of aluminum honeycomb materials. J Sandw Struct Mater 2008;10:133–60. <https://doi.org/10.1177/1099636207078647>.
- [3] Hu LL, Yu TX. Dynamic crushing strength of hexagonal honeycombs. Int J Impact Eng 2010;37:467–74. <https://doi.org/10.1016/j.ijimpeng.2009.12.001>.
- [4] Shen CJ, Lu G, Yu TX. Dynamic behavior of graded honeycombs - a finite element study. Compos Struct 2013;98:282–93. <https://doi.org/10.1016/j.compstruct.2012.11.002>.
- [5] Evans KE, Alderson KL. Auxetic materials: the positive side of being negative. Eng Sci Educ J 2000;9:148–54. <https://doi.org/10.1049/esej:20000402>.
- [6] Ren X, Das R, Tran P, Ngo TD, Xie YM. Auxetic metamaterials and structures: a review. Smart Mater Struct 2018;27:023001. <https://doi.org/10.1088/1361-665X/aaa61c>.
- [7] Lim T-C. Introduction. Auxetic Mater. Struct. Springer: Springer Singapore; 2015. p. 1–43. <https://doi.org/10.1007/978-981-287-275-3>.
- [8] Lakes R. Foam structures with a negative Poisson's ratio. Science 1987;235:1038–40. <https://doi.org/10.1126/science.235.4792.1038>.

- [9] Johnston R, Kazancı Z. Analysis of additively manufactured (3D printed) dual-material auxetic structures under compression. *Addit Manuf* 2021;38. <https://doi.org/10.1016/j.addma.2020.101783> [101783].
- [10] Günaydin K, Rea C, Kazancı Z. Energy absorption enhancement of additively manufactured hexagonal and re-entrant (auxetic) lattice structures by using multi-material reinforcements. *Addit Manuf* 2022;59. <https://doi.org/10.1016/j.addma.2022.103076> (Part A)[103076].
- [11] Simpson J, Kazancı Z. Crushing investigation of crash boxes filled with honeycomb and re-entrant (auxetic) lattices. *Thin-Walled Struct* 2020;150:106676. <https://doi.org/10.1016/j.tws.2020.106676>.
- [12] Zhang X-C, Ding H-M, An L-Q, Wang X-L. Numerical investigation on dynamic crushing behavior of auxetic honeycombs with various Cell-Wall angles. *Adv Mech Eng* 2014;1–12.
- [13] Günaydin K, Eren Z, Kazancı Z, Scarpa F, Grande AM, Türkmen HS. In-plane compression behavior of anti-tetrachiral and re-entrant lattices. *Smart Mater Struct* 2019;28:115028. <https://doi.org/10.1088/1361-665X/ab47c9>.
- [14] Alomarah A, Masood SH, Sbarski I, Faisal B, Gao Z, Ruan D. Compressive properties of 3D printed auxetic structures: experimental and numerical studies. *Virtual Phys Prototyp* 2020;15:1–21. <https://doi.org/10.1080/17452759.2019.1644184>.
- [15] Ingrole A, Hao A, Liang R. Design and modeling of auxetic and hybrid honeycomb structures for in-plane property enhancement. *Mater Des* 2017;117:72–83. <https://doi.org/10.1016/j.matdes.2016.12.067>.
- [16] Zied K, Osman M, Elmahdy T. Enhancement of the in-plane stiffness of the hexagonal re-entrant auxetic honeycomb cores. *Phys Status Solidi* 2015;252:2685–92. <https://doi.org/10.1002/pssb.201552164>.
- [17] Fu M-H, Chen Y, Hu L-L. A novel auxetic honeycomb with enhanced in-plane stiffness and buckling strength. *Compos Struct* 2017;160:574–85. <https://doi.org/10.1016/j.compstruct.2016.10.090>.
- [18] Yang L, Harrysson O, West H, Cormier D. Mechanical properties of 3D re-entrant honeycomb auxetic structures realized via additive manufacturing. *Int J Solids Struct* 2015;69–70:475–90. <https://doi.org/10.1016/j.ijsolstr.2015.05.005>.
- [19] Chen Y, Fu M-H. A novel three-dimensional auxetic lattice meta-material with enhanced stiffness. *Smart Mater Struct* 2017;26:105029. <https://doi.org/10.1088/1361-665X/aa819e>.
- [20] Qiao J, Chen CQ. Analyses on the in-plane impact resistance of auxetic double arrowhead honeycombs. *J Appl Mech* 2015;82:051007. <https://doi.org/10.1115/1.4030007>.
- [21] Qiao JX, Chen CQ. Impact resistance of uniform and functionally graded auxetic double arrowhead honeycombs. *Int J Impact Eng* 2015;83:47–58. <https://doi.org/10.1016/j.ijimpeng.2015.04.005>.
- [22] Wang X-T, Wang B, Wen Z-H, Ma L. Fabrication and mechanical properties of CFRP composite three-dimensional double-arrow-head auxetic structures. *Compos Sci Technol* 2018;164:92–102. <https://doi.org/10.1016/j.compscitech.2018.05.014>.
- [23] Gao Q, Wang L, Zhou Z, Ma ZD, Wang C, Wang Y. Theoretical, numerical and experimental analysis of three-dimensional double-V honeycomb. *Mater Des* 2018;139:380–91. <https://doi.org/10.1016/j.matdes.2017.11.024>.
- [24] Gao Q, Ge C, Zhuang W, Wang L, Ma Z. Crashworthiness analysis of double-arrowed auxetic structure under axial impact loading. *Mater Des* 2019;161:22–34. <https://doi.org/10.1016/j.matdes.2018.11.013>.
- [25] Quan C, Han B, Hou Z, Zhang Q, Tian X, Lu TJ. 3d printed continuous fiber reinforced composite auxetic honeycomb structures. *Compos Part B Eng* 2020;187:107858. <https://doi.org/10.1016/j.compositesb.2020.107858>.
- [26] Sugiyama K, Matsuzaki R, Ueda M, Todoroki A, Hirano Y. 3D printing of composite sandwich structures using continuous carbon fiber and fiber tension. *Compos Part A Appl Sci Manuf* 2018;113:114–21. <https://doi.org/10.1016/j.compositesa.2018.07.029>.
- [27] Chen Y, He Q. 3D-printed short carbon fibre reinforced perforated structures with negative Poisson's ratios: Mechanisms and design. *Compos Struct* 2020;236:111859. <https://doi.org/10.1016/j.compstruct.2020.111859>.
- [28] Markforged, Eiger software, 2022. (<https://www.eiger.io/>). Accessed date: 24/11/2022.
- [29] Yazdani Sarvestani H, Akbarzadeh AH, Niknam H, Hermenean K. 3D printed architected polymeric sandwich panels: Energy absorption and structural performance. *Compos Struct* 2018;200:886–909. <https://doi.org/10.1016/j.compstruct.2018.04.002>.
- [30] ASTM International. ASTM D695-10, Standard test method for compressive properties of rigid plastics. West Conshohocken, PA: 2010.
- [31] Markforged Inc. Material specifications 2019. https://static.markforged.com/markforged_composites_datasheet.pdf. Accessed date January 01/01/2019.
- [32] International Organization for Standardization. ISO 13314:2011(E) Mechanical testing of metals - Ductility testing - compression test for porous and cellular metals. Geneva, CH: 2011.
- [33] ABAQUS/CAE 2017, Simulia, 2022. <https://www.3ds.com/products-services/simulia/products/abaqus>. Accessed date: 02/02/2022.